

Ultrafine-Grained Aluminum Processed by a Combination of Hot Isostatic Pressing and Dynamic Plastic Deformation: Microstructure and Mechanical Properties

G. DIRRAS, T. CHAUVEAU, A. ABDUL-LATIF, J. GUBICZA, S. RAMTANI, Q. BUI, Z. HEGEDŰS, and B. BACROIX

Commercial-purity (99 wt pct), bulk, ultrafine-grained aluminum samples were produced by a two-step process that combines powder consolidation by hot isostatic pressing and dynamic plastic deformation. The compaction step yielded crystallographic texture-free specimens with an average grain size of approximately 2 μm . Then, some of the consolidated specimens were deformed dynamically at room temperature at an initial strain rate of 370 seconds⁻¹ and up to an axial strain of $\varepsilon = 1.25$. After dynamic plastic deformation, the grain size and the dislocation density were approximately 500 nm and 10^{14} m^{-2} , respectively. The yield strength was approximately 77 MPa for the as-consolidated sample, which increased up to approximately 103 MPa and 120 MPa for the impacted samples along the axial and radial directions, respectively. The compression stress as a function of strain showed saturation behavior for the axially deformed samples, whereas the specimens deformed along the radial direction exhibited significant strain softening. The latter behavior is explained mainly by the weakening of the crystallographic texture that occurred because of the strain-path change along the radial direction.

DOI: 10.1007/s11661-011-1028-x

© The Minerals, Metals & Materials Society and ASM International 2011

I. INTRODUCTION

BULK ultrafine-grained (UFG) metals with grain sizes in the submicron range have been at the center of intense study in recent years because of their unique mechanical and physical properties.^[1] Within the framework of producing light and mechanically resistant structures, UFG aluminum and their alloys have been produced routinely by various methods, including quasi-static severe plastic deformation (SPD). The most important SPD procedures are high-pressure torsion (HPT),^[2] equal-channel angular pressing (ECAP),^[3] accumulative roll bonding (ARB),^[4] multidirectional forging (MDF),^[5] and the combinations of these processes, such as ECAP + HPT.^[6] In most SPD methods, the reduction of the grain size occurs via the formation of subgrains or cells bounded by low-angle grain boundaries (LAGBs), which subsequently transform into high-angle grain boundaries (HAGBs) with subsequent straining.^[7] In the ECAP method, the rate of transformation from LAGBs to HAGBs depends on the

processing route. For example, equiaxed UFG grains with high fractions of HAGBs formed already after four ECAP passes applying route B_C , whereas in the case of route A, many more passes were needed to reach the same state.^[3]

Recently, SPD methods applied at high strain rates and at cryogenic or ambient temperatures have also been used to produce UFG microstructures in face-centered cubic (fcc) materials such as Cu and Ni.^[8] These procedures are referred to as dynamic (severe) plastic deformation (DPD) methods. It was reported that during DPD at cryogenic temperatures, grain refinement was promoted by an additional mechanism of nucleation of twin bundles, which are subsequently fragmented by the passage of adiabatic shear bands.^[9] Under a subsequent quasi-static uniaxial tensile or compression deformation at room temperature (RT), the high dislocation density (10^{15} to 10^{16} m^{-2}) formed at cryogenic temperatures yields flow stress stagnation and eventually strain softening as a result of recovery. In such a case, plastic instability might occur and result in limited tensile ductility.^[10,11]

Powder metallurgy (PM) methods such as hot isostatic pressing (HIP) and spark plasma sintering (SPS) can produce bulk UFG metals and alloys starting from nanopowders.^[12-16] The as-processed UFG materials have high fractions of HAGBs and random crystallographic texture.^[14,17] However, some inherent weaknesses of the consolidated materials are often observed, such as incomplete particle bonding or residual porosity, which usually lead to easier crack formation during straining. The application of high temperature during

G. DIRRAS, B. BACROIX, and S. RAMTANI, Professors, T. CHAUVEAU, Research Engineer, and Q. BUI, PhD, are with the LSPM, UPR CNRS 3407, Université Paris 13, 93430 Villetaneuse, France. Contact e-mail: dirras@univ-paris13.fr A. ABDUL-LATIF, Professor, is with the Laboratoire d'Ingénierie des Systèmes Mécaniques et des Matériaux, 93407 St Ouen Cedex, France. J. GUBICZA, Associate Professor, and Z. HEGEDŰS, PhD Student, are with the Department of Materials Physics, Eötvös Loránd University, Budapest H-1518, Hungary.

Manuscript submitted January 21, 2011.

Article published online December 21, 2011

sintering may result in better consolidation properties, but naturally it leads to grain growth. More importantly, the contamination of the starting nanopowders because of their high specific surface area is a major issue that has a dramatic impact on the mechanical properties of the consolidated materials.^[18,19] Unlike in nanopowders, in conventional micrometer-sized powders, the problems mentioned previously are diminished because the powders have low specific surface area and reactivity, which also facilitate their handling in powder metallurgy processing. Therefore, contamination-free and fully dense products have been processed routinely from coarse-grained powders, although their microstructure is hardly of the UFG type.

In this paper, we report on the processing of bulk UFG aluminum by a method that combines the advantages of PM and DPD routes. To minimize the contamination introduced by the powder into the bulk samples, conventional micrometer-sized powder particles are first consolidated by HIP. Then, the grains of the sintered material are subsequently refined by DPD performed at RT. The obtained microstructure and its long-term stability at RT are fully characterized by transmission electron microscopy (TEM), X-ray texture measurement, and X-ray line profiles analysis (XLP). The mechanical behavior of the UFG microstructure processed by the combination of HIP and DPD is investigated by means of a quasi-static compression test at RT with the deformation axis parallel or perpendicular to the impact direction. The underlying deformation mechanisms are deduced from postmortem TEM investigations complemented by XLP and crystallographic texture evolution. The influence of the strain-path change on the microstructure and texture stability during straining is discussed.

II. EXPERIMENTAL PROCEDURES

The starting material used was a commercial purity (99 wt pct) aluminum powder supplied by POUDMET S.A.S (Bailleval, France), whose microstructure is shown in the scanning electron microscopy (SEM) image in Figure 1. The powder consisted of particles with a mean size of approximately 5 μm agglomerated into clusters 50 to 100 μm in size. The chemical composition of this powder is shown in Table I.

The powder was consolidated by HIP under the following optimized conditions: a heating rate of 375 K/h, a dwell pressure of 200 MPa, and a temperature of 723 K (450 °C). The HIP cycle was stopped after 240 minutes when the built-in dilatometer indicated that there was no more capsule deformation, meaning that the sample was fully compacted. The HIP temperature was selected to be the optimum value that gives a relative mass density higher than 99 pct without the occurrence of considerable grain growth. HIP process resulted in a cylinder-shaped sample approximately 12 mm in diameter and 70 mm in height. It is noted that the current material is the same as that studied in Reference 20. Usually, the surface of Al powder particles are covered by an amorphous, oxygen-rich thin film that may transform into crystalline alumina during high-temperature sintering. In the samples used in this study, oxide peaks were not observed in the X-ray diffraction patterns measured after consolidation. This experimental result does not exclude the existence of a small amount of crystalline or amorphous oxide or hydroxide in the HIP-processed samples. However, even if this phase exists, it does not alter the conclusions of the current study. From the HIP-processed specimens, samples 12 mm in diameter and 21 mm in height were

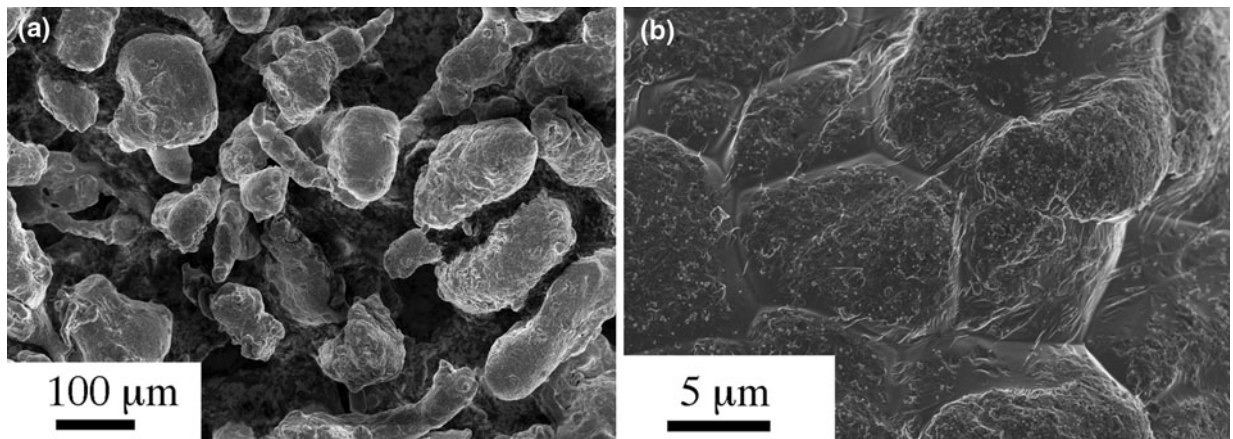


Fig. 1—(a) SEM image of commercial purity (99 wt pct) aluminum powder used for HIP processing. (b) SEM image with higher magnification reveals that the clusters with the size of 50 to 100 μm in (a) consisted of particles having a mean size of approximately 5 μm .

Table I. Chemical Composition of the HIP-Processed Al Sample Obtained by Inductively Coupled Plasma/Optical Emission Spectrometry

| Elements | Al | Ca | Cu | Fe | Mg | Mn | S | Si |
|-------------------|------|-----------|---------|----------|----------|---------|----|------------|
| Composition (ppm) | base | 1175 ± 20 | 303 ± 5 | 1069 ± 5 | 944 ± 15 | 166 ± 4 | <8 | 5735 ± 112 |

cut and submitted to DPD using a drop mass bench as described in previous studies.^[20,21] After impact, the sample was deformed into a disk shape 22.5 mm in diameter and 6 mm in height (Figure 2), corresponding to an axial strain of approximately 1.25. During DPD, the impact velocity decreases gradually with increasing strain down to a zero value. In the current experiment, the initial velocity was 7.8 m/s. The strain rate $\dot{\epsilon}$ at any moment of DPD can be given by the actual velocity v and the height of the sample l using the following formula:

$$\dot{\epsilon} = \frac{d}{dt} \left(\ln \frac{l_0}{l} \right) = \frac{1}{l} \left| \frac{dl}{dt} \right| = \frac{v}{l} \quad [1]$$

where l_0 is the initial height of the specimen (21 mm). According to Eq. [1], the initial strain rate was 370 seconds⁻¹. The DPD-processed specimens were studied by quasi-static compression tests conducted on prismatic samples with dimensions of 3 mm × 3 mm × 5 mm at RT and a strain rate of 1.8×10^{-4} seconds⁻¹.^[20] The strain in the quasi-static compression tests was determined from the crosshead displacement as $\epsilon = \ln \left(\frac{l_0}{l} \right)$. In the calculation of the plastic strain, the collective elastic stiffness of the machine and the sample was determined from the initial elastic deformation and used in the subtraction of the elastic component from the total strain. Lubrication was not used during DPD or during quasi-static compression tests. However, barreling of the

samples was not observed (the samples were prismatic specimens with the dimensions of 3 mm × 3 mm × 5 mm). At the same time, twisting of the samples was observed when the total strain exceeded 60 pct. Two directions of the compression axis relative to the impact direction were considered, namely the axial direction X_1 and the radial direction X_2 parallel and perpendicular to the impact direction, respectively (Figure 2). It should be noted that immediately after the deformation procedures (DPD and subsequent quasi-static compression tests), the samples were stored in a freezer until microstructure investigations were conducted to prevent the recovery of the deformed microstructures.

Microstructural investigations were carried out by means of complementary techniques including TEM, texture analysis, and XLP. For TEM investigations, thin foils were prepared from the samples processed by HIP, HIP + DPD and quasi-static compression. Initially, disks 3 mm in diameter and 70 μm in thickness were cut using an Ultrasonic Disc Cutter Model 601 (Gatan, Inc., Pleasanton, CA) and dimpled using a Gatan Model 656 Dimple Grinder. The final thinning was carried out using a Gatan Precision Ion Polishing System Model 691 under the following conditions: electrical tension of 5 kV, current of 5 mA, and beam inclination angle of ± 7 deg. TEM investigations were carried out on a JEOL 2011 EM operating at 200 kV (JEOL, Ltd., Tokyo, Japan).

The grain boundary misorientation distribution on the impacted surface of the HIP + DPD sample was investigated by electron backscattering diffraction (EBSD). The EBSD experiments were carried out using a Zeiss Supra 40VP FEG scanning electron microscope (Carl Zeiss, Oberkochen, Germany). The scans covered regions of approximately 150 μm × 150 μm using a step size between neighboring measurement positions of 0.2 μm . The grain boundary misorientation distribution was extracted from the EBSD scan with OIM software version 4 (TexSem Laboratories, Mesa, AZ).

The crystallographic texture was studied after DPD by X-ray diffraction (XRD) on the faces lying perpendicular and parallel to the impact direction, which are denoted as faces (1) and (2), respectively. To describe the results, it was necessary to attach an orthogonal reference system to each analyzed face. The axes of these systems are denoted as $X1_i$, $X2_i$, and $X3_i$ ($i = 1, 2$), respectively, where i stands for the face being investigated. $X1_i$ is perpendicular, whereas $X2_i$ and $X3_i$ are parallel, to the face (i). Figure 3 illustrates these two reference systems. The texture measurements were performed using an Inel four circles diffractometer (Inel, Inc., Stratham, NH) in Bragg-Brentano geometry with a CoK α point focus X-ray source ($\lambda = 0.17902$ nm). The pole figures corresponding to {111}, {200}, and {220} reflections were determined. After correcting the experimental pole figures (background, defocusing, and normalization), the orientation distribution function was calculated using Labotex software (LaboSoft s.c., Krakow, Poland).^[22] In addition, crystallographic texture investigations were also performed after quasi-static compression tests on the faces perpendicular to the compression axes of the prismatic samples.

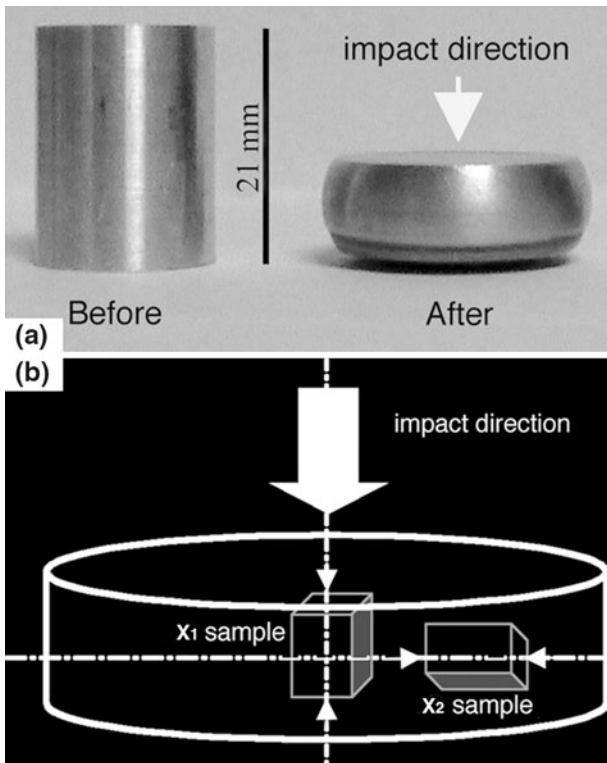


Fig. 2—(a) The HIP-processed specimen before and after room-temperature DPD. (b) Schematic drawing of samples X_1 and X_2 used for the quasi-static compression tests (b). The large arrow indicates the impact direction, whereas the small arrows indicate the subsequent quasi-static compression tests axes.

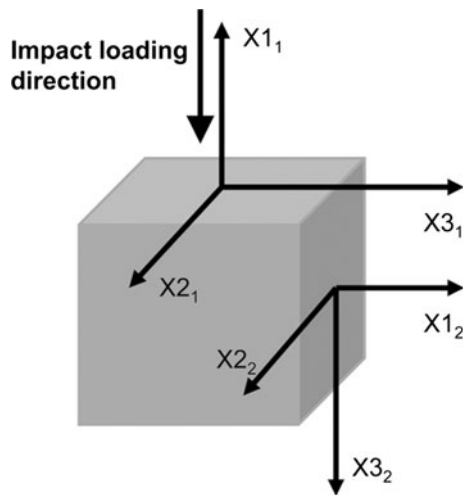


Fig. 3—Details of the reference systems attached to faces (1) and (2) of the DPD-processed samples used for X-ray analyses and compression tests.

The X-ray line profiles were measured by a high-resolution rotating anode diffractometer (Nonius, FR591; BRUKER AXS, Delft, the Netherlands) using $\text{CuK}\alpha_1$ radiation ($\lambda = 0.15406 \text{ nm}$). The line profiles were evaluated using the convolutional multiple whole profile (CMWP) fitting procedure described in detail in other reports.^[23,24] In this method, the experimental pattern is fitted by the convolution of the instrumental pattern and the theoretical size and strain line profiles. The theoretical profile functions used in this fitting procedure are calculated based on a model of the microstructure, in which the crystallites have spherical shape and lognormal size distribution, and the lattice strains are assumed to be caused by dislocations. This method gives the area-weighted mean crystallite size and the dislocation density with good statistics. An example of fitting obtained for the sample processed by DPD is shown on a logarithmic intensity scale in Figure 4. The measurements were carried out on face (1) of the HIP + DPD samples and were repeated after storing the sample at RT for 3 months to check the stability of the microstructure.

III. RESULTS AND DISCUSSION

A. Microstructure Investigations

1. Analysis of the microstructure by TEM

The TEM image in Figure 5 shows that after HIP, the microstructure consists of equiaxed grains with a mean grain size of approximately $2 \mu\text{m}$. After the HIP + DPD procedure, the microstructures shown in Figures 6(a) and (b) were observed on faces (1) and (2), respectively. The grains are equiaxed when viewed along the face lying perpendicular to the impact direction (face (1) and slightly elongated in a direction perpendicular to the impact axis when viewed along the face lying parallel to the impact direction (face (2)). The mean grain size is approximately 500 nm , which is approximately four

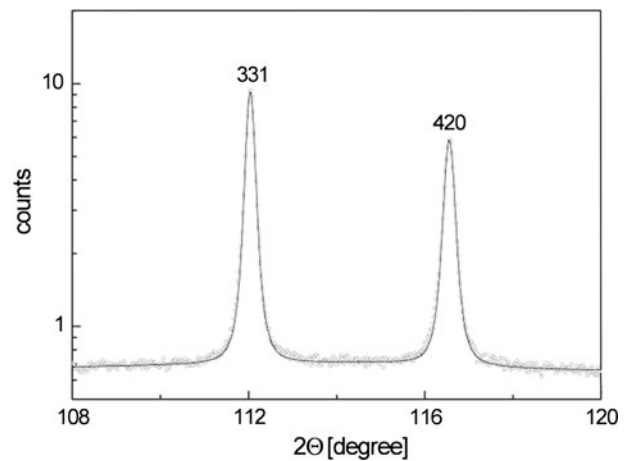


Fig. 4—A part of the experimental X-ray diffraction pattern (open circles) and the fitted curve (solid line) obtained by CMWP fitting method on the sample processed by the combination of HIP and DPD procedures.

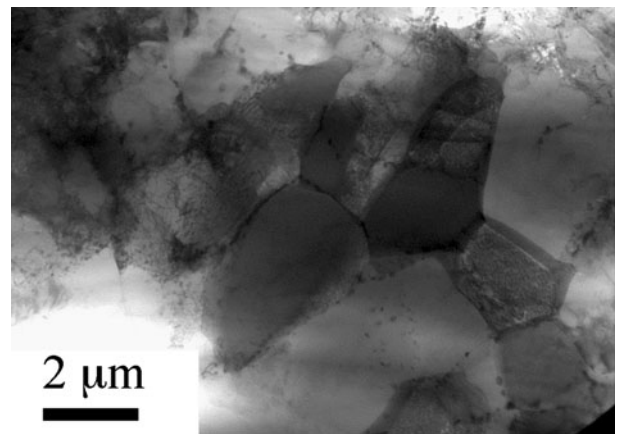


Fig. 5—TEM image showing the microstructure after HIP-processing that consists of equiaxed grains with a mean grain size of approximately $2 \mu\text{m}$.

times lower than the initial value obtained immediately after HIP. Finally, incidental dislocations within the grain/subgrain interiors are scarcely observed. These features of the microstructure suggest strongly that a recovery phenomenon occurred in the course of DPD processing because of the high strain rate. It is worth noting that even if a possible associated increase in the temperature on dynamic straining has not been demonstrated explicitly in the current work, RT ($\sim 298 \text{ K}$ [$25 \text{ }^\circ\text{C}$]) already corresponds to a homologous temperature of $\sim 0.32T_m$ (where T_m is the melting temperature of Al with a value of 933 K [$660 \text{ }^\circ\text{C}$]), which is close to the lower bound of the recrystallization temperature range of pure metals (approximately $0.4T_m$). Actually, similar microstructures were reported to form during cold rolling and ECAP of aluminum and its alloys,^[25–27] or during high-strain-rate load impacts in Ni.^[28] In addition, a similar microstructure with sharp boundaries and dislocation-free interiors as has been reported previously during the static annealing of Al + 0.13

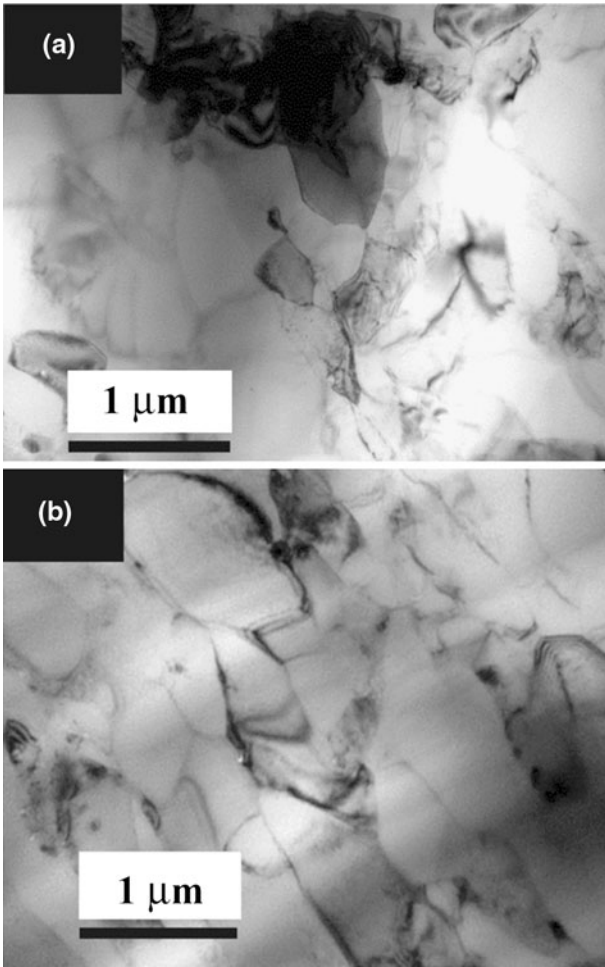


Fig. 6—TEM micrographs showing the microstructure of the samples processed by HIP + DPD: (a) TEM view on face (1) (perpendicular to X_{11}) and (b) TEM view on face (2) (perpendicular to X_{12}).

wt pct Mg alloy at 423 K (150 °C). The alloy was deformed initially by plane strain compression in liquid nitrogen.^[29] Figure 7(a and b) show an EBSD image obtained along the impacted surface of the HIP + DPD sample and the corresponding boundary misorientation distribution, respectively. Although all orientations seem to be present in the EBSD image, a tendency toward the [011] orientation is observed. Additionally, Figure 7(b) reveals a high fraction of LAGBs (approximately 60 pct).

The temperature and strain rate of SPD processing have a significant effect on the grain size in nanocrystalline or ultrafine-grained metals and alloys. For a given strain and processing method, the higher the strain rate and/or lower the temperature of deformation, the smaller the grain size. The combined effects of the strain rate and temperature can be expressed by the Zener-Hollomon parameter defined as^[30]

$$Z = \dot{\epsilon} \exp\left(\frac{Q}{RT}\right) \quad [2]$$

where $\dot{\epsilon}$ is the strain rate in unit of seconds⁻¹, R is the gas constant $\left(8.314 \frac{\text{J}}{\text{molK}}\right)$, T is the absolute

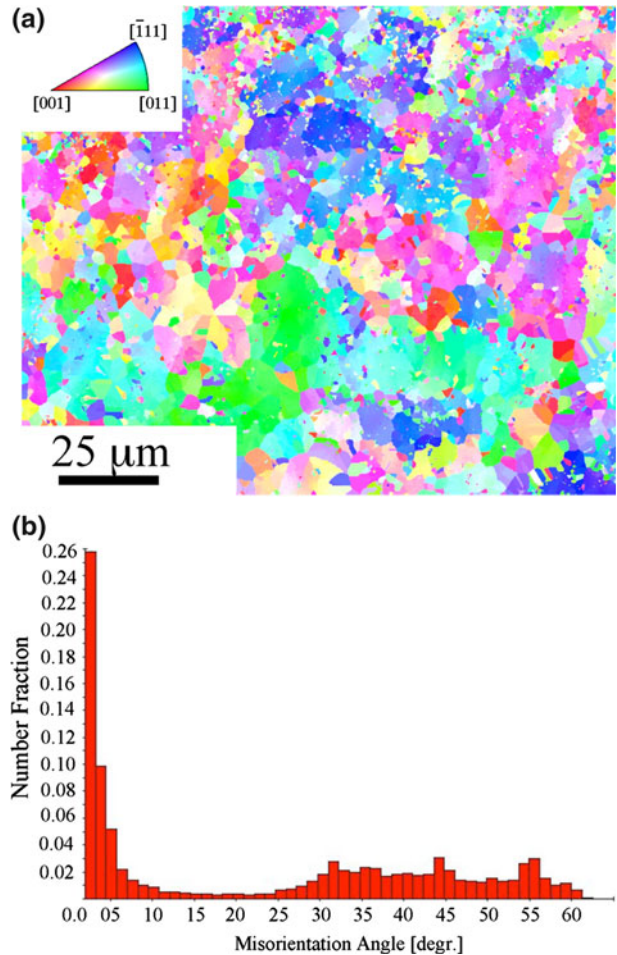


Fig. 7—(a) EBSD image obtained on the impacted surface of the HIP + DPD sample and (b) the corresponding boundary misorientation distribution.

temperature, and Q is the activation energy for diffusion. For Al – 1 wt pct Mn, the following relationship between the grain size (d) and parameter Z is suggested^[31]:

$$d^{-1} = 0.045 \ln Z - 0.76 \quad [3]$$

where d is given in μm . The higher the value of Z , the smaller the grain size obtained during SPD processing. During DPD processing, the strain rate decreases from 370 seconds⁻¹ to 0 seconds⁻¹. Substituting a mean strain rate of 185 seconds⁻¹ and an activation energy of 156 kJ/mol^[31] into Eq. [2], $\ln Z = 68$ is obtained. Using this value, $d = 435$ nm is calculated from Eq. [3], which is close to the grain size determined experimentally by TEM (500 nm), despite the different compositions of the current alloy and the material for which Eq. [3] had been obtained.

2. Crystallographic texture analysis after HIP + DPD

The recalculated pole figures measured on faces (1) and (2) are shown in Figures 8(a) and (b), respectively. The analysis of the pole figures obtained on face (1) highlights a $\langle 220 \rangle$ -fiber texture denoted as B ($\langle 220 \rangle$ preferential orientation along X_{11} and isotropy in the

($X2_1$, $X3_1$) plane). This is indeed the classic texture found after uniaxial compression in fcc materials. In the current case, isotropy is not complete and a reinforcement of this fiber texture is found close to the component denoted as A, which can be identified as being of the $\{124\}\langle 232 \rangle$ type. Figure 8(b) shows that the texture components A and B are also present on face (2) but with lower intensities than the texture measured on face (1), indicating some through-thickness texture inhomogeneity of the impacted sample. To investigate this issue, the pole figures obtained from face (1) (Figure 8(a)) were rotated by 90 deg around $X2_1$ (plotted in Figure 8(c)) and compared with the pole figures obtained from face (2) (Figure 8(b)). The comparison reveals that whereas the texture components A and B are still present in Figure 8(c), the overall pole figures deviate strongly from those shown in Figure 8(b). This result strongly suggests through-thickness texture heterogeneity exists as a consequence of DPD processing.

3. Line profile analysis after HIP + DPD procedure

The results of an X-ray line profile analysis are summarized in Table II.

The dislocation density obtained immediately after HIP + DPD processing ($1.5 \pm 0.2 \times 10^{14} \text{ m}^{-2}$) is close to the saturation dislocation density ($1.8 \pm 0.3 \times 10^{14} \text{ m}^{-2}$) achieved by the ECAP method in 4N-purity Al at RT.^[32] At the same time, the mean crystallite size after HIP + DPD ($174 \pm 15 \text{ nm}$) is smaller than the saturation value obtained by ECAP ($272 \pm 30 \text{ nm}$ ^[32,33]) similarly to the grain size, which is

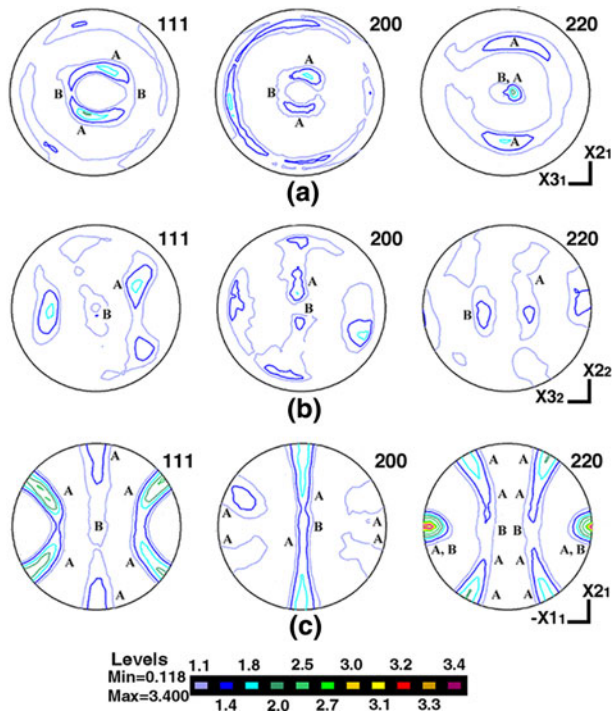


Fig. 8—Recalculated pole figures showing the measured textures: (a) on face (1) and (b) on face (2). The pole figures in (a) were rotated by 90 deg around $X2_1$ and plotted in (c). See text for more details.

approximately 500 nm after HIP + DPD and approximately $1 \mu\text{m}$ for the ECAP-processed sample. The smaller grain and crystallite sizes in the current case can be explained by the higher pinning effect of the larger impurity content in grain boundaries. It is noted that the smaller crystallite size measured by an X-ray line profile analysis compared with the grain size obtained by TEM is a typical phenomenon in severely deformed metals.^[32] This can be attributed to the fact that the crystallites are the domains in the microstructure, which scatter X-rays coherently. Because the coherency of X-rays is broken even if they are scattered from volumes with small misorientations (1 to 2 deg), the crystallite size corresponds to the subgrain size in severely deformed microstructures.^[32] In addition, Table II indicates that this mean crystallite size remained unchanged within the experimental error during the quasi-static compression test or during the storage of the samples after DPD processing. The dislocation density decreased only slightly during storage for 3 months at RT. The recrystallization is prevented by the total impurity content, 1.2 wt pct, calculated from Table I. Therefore, the HIP + DPD procedure seems to be an efficient method for processing stable UFG Al in a short time.

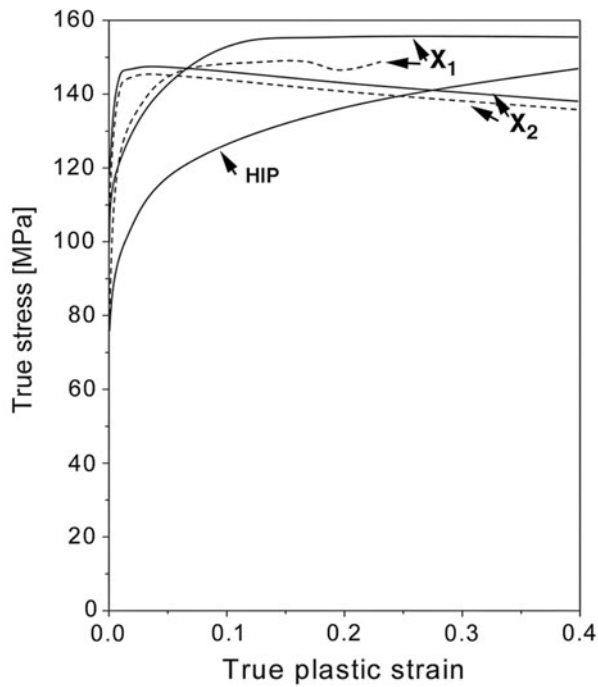
B. Mechanical Properties in Quasi-Static Compression Conditions

1. Macroscopic description of the mechanical behavior

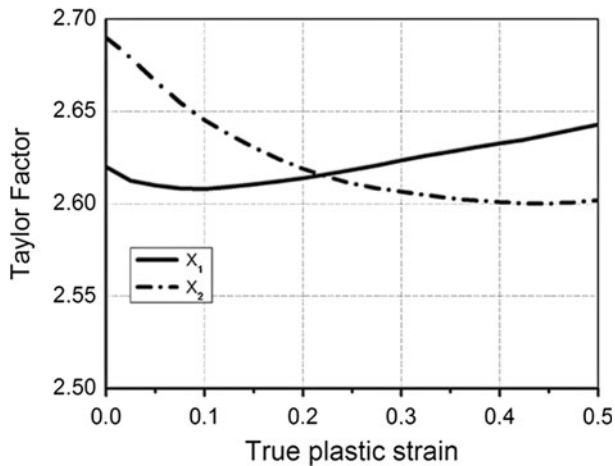
The solid curves in Figure 9(a) show the true stress–true plastic strain (limited to a plastic strain of $\epsilon = 0.4$) data for the DPD-processed and the HIP-consolidated samples obtained by quasi-static compression testing at RT and at a strain rate of $1.8 \times 10^{-4} \text{ seconds}^{-1}$. Samples X_1 and X_2 were compressed along axes parallel and perpendicular to the impact direction, respectively (Figure 2). To illustrate the reproducibility of the compression measurements, additional disk samples were fabricated from the DPD-processed disk in the same way that specimens X_1 and X_2 were created. These complementary stress–strain data are shown as dashed curves in Figure 9(a). In the following, only the stress–strain curves represented by the solid curves are evaluated in detail because the microstructures of these specimens were investigated in the previous sections. Sample X_1 exhibits a long hardening regime followed by

Table II. The Parameters of the Microstructure Obtained by X-Ray Line Profile Analysis

| Sample | Mean Crystallite Size | Dislocation Density |
|---------------------------------|-------------------------|---|
| HIP + DSPD | $174 \pm 15 \text{ nm}$ | $(1.5 \pm 0.2) \times 10^{14} \text{ m}^{-2}$ |
| HIP + DSPD after 3 months at RT | $149 \pm 15 \text{ nm}$ | $(1.0 \pm 0.2) \times 10^{14} \text{ m}^{-2}$ |
| Compressed in X_1 direction | $175 \pm 15 \text{ nm}$ | $(1.2 \pm 0.2) \times 10^{14} \text{ m}^{-2}$ |
| Compressed in X_2 direction | $176 \pm 15 \text{ nm}$ | $(1.0 \pm 0.2) \times 10^{14} \text{ m}^{-2}$ |



(a)



(b)

Fig. 9—(a) Mechanical behavior under quasi-static compression tests at a strain rate of $\sim 1.8 \times 10^{-4}$ seconds $^{-1}$ for samples X_1 and X_2 . The solid and dashed curves illustrate the reproducibility of the stress-strain data. For comparison, the behavior of the specimen processed by HIP is also shown. (b) The geometrical hardening evolution in term of Taylor factor, M along directions X_1 and X_2 .

a flow stress plateau, unlike sample X_2 , which softens immediately after a short stress plateau. The yield strength of sample X_2 (~ 120 MPa) is slightly higher than that of sample X_1 (~ 103 MPa); nevertheless, the maximum flow stress values for the two specimens are close to each other (148 and 156 MPa, respectively). Because of the softening exhibited by sample X_2 , the flow stress at a plastic strain of 0.4 is smaller (~ 137 MPa) than the corresponding value for sample X_1 (~ 156 MPa). The yield strength was calculated from the grain size (500 nm) by the Hall-Petch equation for Al using a friction strength of $\sigma_0 = 11$ MPa and a Hall-Petch

slope of $k_H = 115 \text{ MPa } \mu\text{m}^{1/2}$.^[34] The experimental yield strength is lower than the value calculated from the Hall-Petch formula (174 MPa). This may be explained by the activity of additional deformation mechanisms besides the dislocation motion in the grain interiors. For instance, the contribution of grain boundary sliding to plasticity even at RT has been proved recently in Al with a grain size of 1 μm .^[35] In the current material, the grain size is even smaller, promoting the occurrence of deformation processes at grain boundaries that may result in the deviation of the yield strength from the value obtained by the Hall-Petch relationship.

A wealth of literature addressed the effect of strain-path change in metals and alloys.^[36–38] Rauch and Schmitt^[39] reported on different situations when simple shear tests were performed on mild steel samples predeformed by tension. The authors showed that the resulting macroscopic behavior depends strongly on the angle (α) between the tensile and the shear directions. In particular, for $\alpha = 90$ deg, the yield strength is maximized and the stress-strain curve then exhibits softening behavior similar to that exhibited by the sample tested along the X_2 direction. This behavior of the mild steel samples was explained by the destabilization of intra-granular structure formed during predeformation.

Such anisotropy in the initial flow stress and work hardening was also reported for the uniaxial loading of UFG metals prestrained by ECAP.^[40–43] For instance, Alexander and Beyerlein^[44] reported on the anisotropy of the mechanical properties of high-purity copper processed by ECAP. The authors showed that the ECAP-processed material was mechanically anisotropic, with a larger compression strength along the transverse direction (using the standard notation for ECAP^[45]) than that along the other directions. In addition, work softening occurred after a strain of approximately 1 pct along this direction, whereas slight but positive work hardening occurred along the other directions; this behavior is similar to that observed here for samples X_2 and X_1 , respectively. The large initial strength along the transverse direction and the subsequent softening may be caused by the “cross effect” of dislocations: The dislocation walls formed along the slip planes that are active during prestrain will act as barriers to the propagation of other slip systems activated after strain-path change.^[46] The subsequent work softening is a consequence of the recovery of the previously formed dislocation structure.^[40] However, this effect is usually transient and followed by a strain hardening at a strain of approximately 0.1 to 0.2. In our case, such a hardening was not observed for sample X_2 up to a strain of 0.4 (Figure 9(a)); therefore, the “cross effect” cannot be the sole reason for the anisotropic mechanical behavior of the current DPD-processed sample.

In our previous paper,^[20] in addition to the material whose behavior is described in this article, another sample was prepared by DPD at a falling mass velocity of 9.2 m/s corresponding to an initial strain rate of 438 seconds $^{-1}$, which is higher than that for the current case. The quasi-static compression stress-strain data for the specimen treated by DPD at an initial strain rate of 438 seconds $^{-1}$ were plotted in Figure 4(b) of Reference 20.

For that sample, softening was observed under quasi-static compression not only along direction X_2 but also along direction X_1 , although the degree of softening was higher for the former direction. The yield strength was larger for both directions in the case of higher DPD strain rate. Most probably, the higher strain rate yielded a much larger dislocation density than the saturation value at RT, which decreased during subsequent quasi-static compression, leading to a softening even along direction X_1 ; this situation is similar to that proposed in Reference 47. Along direction X_2 this effect is superimposed on the effect of strain-path change, leading to a stronger softening.

Among other substructural features that could lead to an orientation dependence of the mechanical response, crystallographic texture anisotropy might also play a significant role.^[37] Indeed, Li^[40] reported that the anisotropy in the initial flow stress can be reasonably related to crystallographic texture.

To determine whether texture might be partially responsible for the differences in the yield strength and the strain hardening between samples X_2 and X_1 , some compression tests were simulated from the measured initial textures with a viscoplastic Taylor model. The calculated Taylor factor M is presented in Figure 9(b) as a function of strain. The value of M for sample X_2 is larger than that for sample X_1 when the compression begins. This is in line with the higher yield strength for the former specimen. Furthermore, the Taylor factors for samples X_2 and X_1 decrease and increase, respectively, with increasing strain, which can explain the softening and hardening during compression along axes X_2 and X_1 , respectively. This indicates that the observed mechanical behaviors are indeed partly caused by the texture. It is noted that the ratio of the two initial M values (1.04) in Figure 9(b) is less than the ratio of the initial measured yield strength values (1.14), suggesting that other phenomena, such as the “cross effect” may also contribute to the anisotropic mechanical behavior of the DPD-processed sample. Furthermore, the difference in the effective grain size along various directions may also affect the material’s strength because the grains are flattened during DPD.

2. Texture evolution analysis of the compressed samples

Figures 10(a) and (b) show the results of crystallographic texture measurements carried out after compression tests at RT up to $\varepsilon \sim 0.5$ along the faces lying perpendicular to the compression axis for samples X_1 and X_2 , respectively. The most striking feature is the strengthening of the texture (in particular component A) for sample X_1 (Figure 10(a)), whereas in sample X_2 the texture weakens and the grain orientations are randomized (Figure 10(b)). As expected (and confirmed by the simulations presented previously), the crystallographic texture (mainly composed of a $\langle 220 \rangle$ fiber) remains stable when the sample is compressed along X_1 (this corresponds to a monotonic loading sequence); meanwhile, it is destabilized when compressed along X_2 (this corresponds to a change in strain path). This strain-path change could also lead to dislocation structure

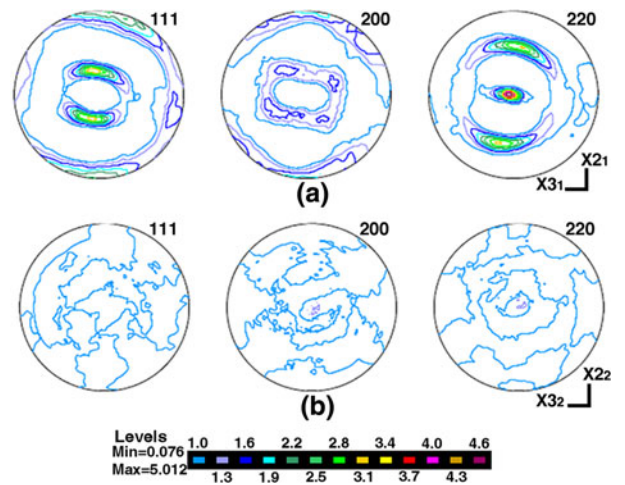


Fig. 10—The crystallographic texture in terms of [111], [200], and [220] pole figures measured after compression on the faces perpendicular to the compression axes for samples X_1 (a) and X_2 (b).

destabilization, which could in turn contribute to macroscopic softening.

3. TEM investigations after quasi-static compression

After quasi-static compression of samples X_1 and X_2 up to a plastic strain of $\varepsilon \sim 0.5$, TEM investigations were carried out on both faces lying perpendicular and parallel to the compression axis. In the case of sample X_1 , the microstructure along the face perpendicular to the compression axis exhibits equiaxed grains (or subgrains) with a balanced mixture of LAGBs and HAGBs (see Figure 11(a)), the latter showing fringe contrasts that are characteristic of recovered/recrystallized microstructures, as reported in.^[48] Figures 11(b) and (c) show the deformation microstructures on a plane lying parallel to the compression axis for sample X_1 . Figure 11(b) illustrates a band of approximately $2 \mu\text{m}$ in thickness that contains ultrafine grains (mean size of approximately 500 nm) whose interiors are populated with dislocations. It is noted that a dislocation-free grain in the center of Figure 11(b) has a highly curved boundary, suggesting that this grain has grown at the expense of the neighboring grains populated by dislocations. Figure 11(c) shows another characteristic feature, namely a band (whose boundaries are indicated by arrows) of equiaxed grains. Outside the band, there are two grains (marked by A and B) with flat interfaces along the band. Actually, the observed microstructure resembles that shown in Figure 6(b); therefore, it is believed to be a fingerprint of substructures introduced by DPD processing. This observation confirms the fact that the DPD microstructure is stable under subsequent straining at RT (similarly to the texture) when the deformation axis is not changed relative to the direction of the former impact test. Therefore, in this case, no work softening as a result of microstructure instability is expected to occur.

Figure 12 illustrates the different features of the deformed microstructures of sample X_2 . The microstructure along the plane perpendicular to the compression axis contains elongated grains (Figure 12(a))

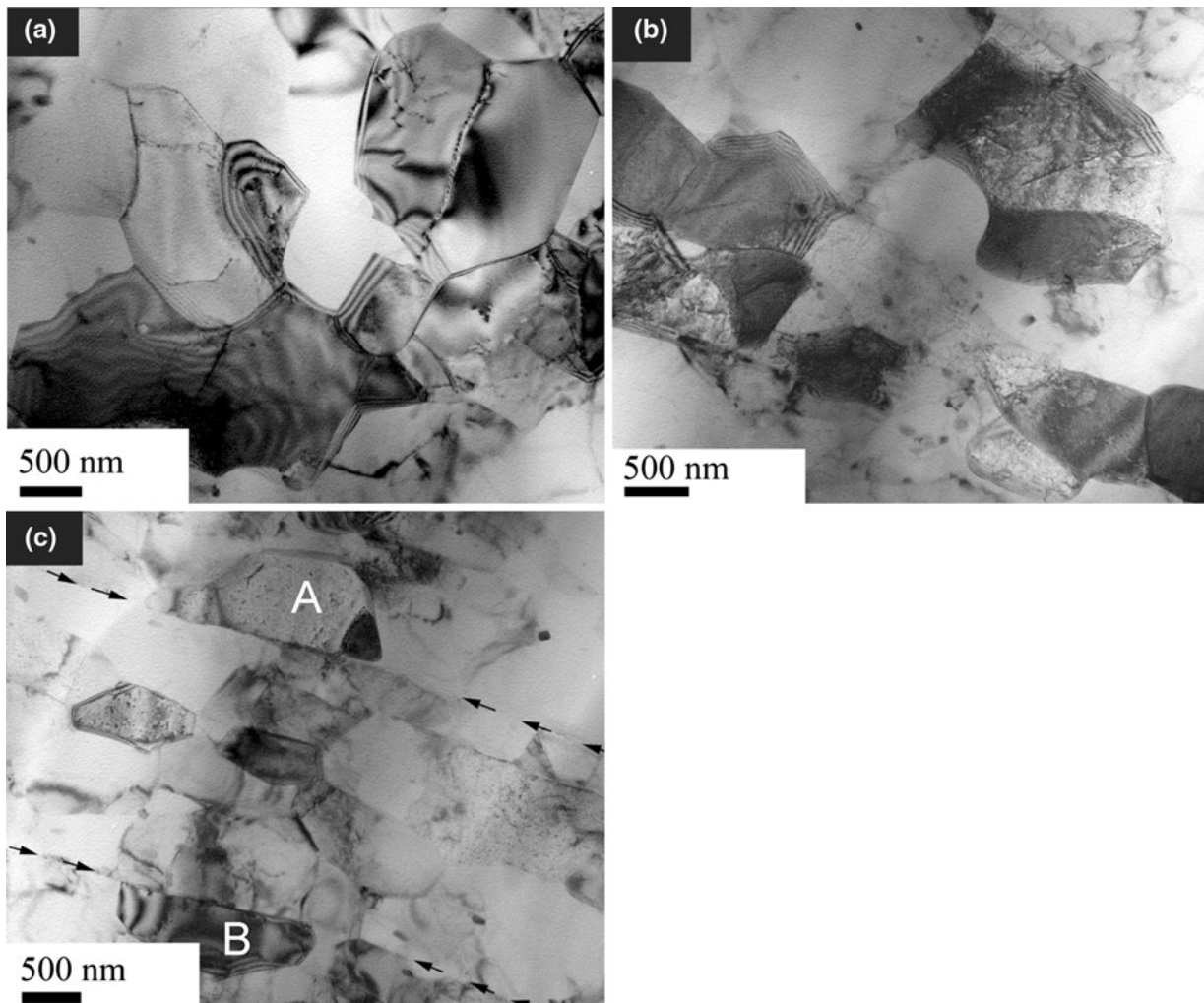


Fig. 11—TEM micrographs obtained after quasi-static compression test for sample X_1 . The thin foils are perpendicular and parallel to the compression axis in (a) and (b, c), respectively.

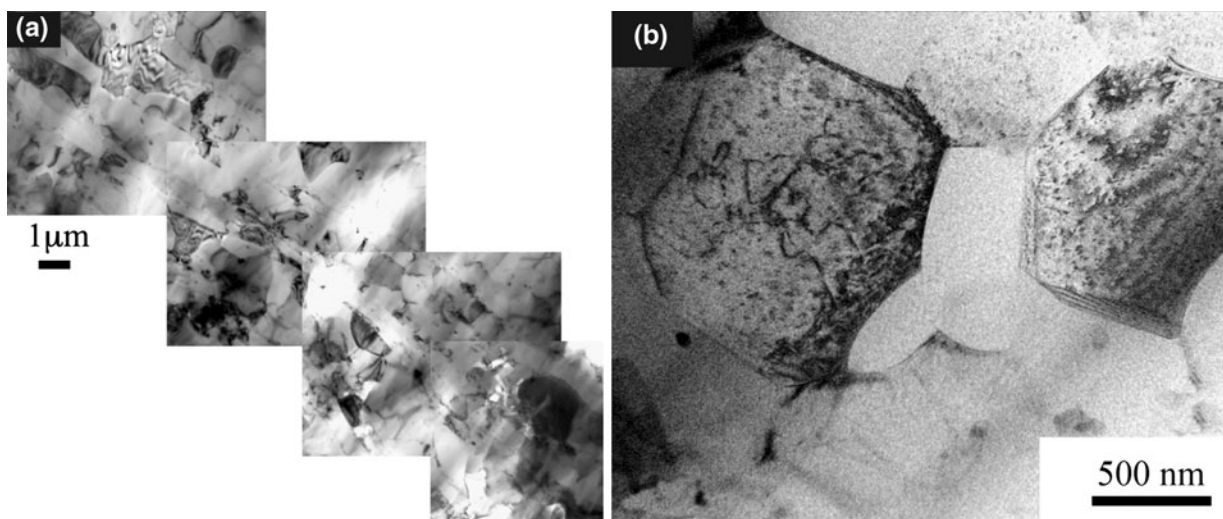


Fig. 12—TEM micrographs obtained after quasi-static compression test for sample X_2 . The thin foils are perpendicular and parallel to the compression axis in figures (a) and (b), respectively.

similar to those observed immediately after DPD processing. The elongated grains are most probably caused by the passage of a shear band. In contrast, the microstructure along a plane parallel to the compression axis consists of exclusively equiaxed grains, as shown in Figure 12(b). In addition, dislocation-free grains with curvature toward the neighboring grains populated by dislocations are also observed in this study. It was reported recently that new grains can develop dynamically because of the pronounced bulging of preexisting grain boundaries caused by high stored energy or an orientation gradient.^[49] Although the occurrence of dynamic recrystallization could not be strictly confirmed here (additional investigations are needed), it can be stated that during deformation after strain-path change, strong strain gradients might develop at grain boundaries in the vicinity of shear bands,^[48] which promote recrystallization during the early stages of deformation. Nevertheless, TEM investigations revealed that the grain structure developed during DPD processing remained stable during subsequent compression; however, limited recovery/recrystallization might occur at shear bands.

IV. CONCLUSIONS

Hot isostatic pressing and dynamic plastic deformation have been combined to produce Al samples with UFG microstructure. The study of the microstructure and the mechanical behavior yielded the following results:

1. The sample consolidated by HIP has an average grain size of 2 μm , which was refined to approximately 500 nm after DPD processing. The latter grain size is smaller than that achieved by ECAP (approximately 1 μm) at room temperature. The combination of HIP and DPD resulted in a UFG microstructure with a strong $\langle 220 \rangle$ -fiber texture. The dislocation density was $1.5 \pm 0.2 \times 10^{14} \text{ m}^{-2}$, which is close to the saturation dislocation density ($1.8 \pm 0.3 \times 10^{14} \text{ m}^{-2}$) achieved by the ECAP method at room temperature. The UFG microstructure obtained by dynamic severe plastic deformation seems to be stable because only a slight decrease in the dislocation density was observed and the grain size remained unchanged during storage for several months at RT.
2. The shape of grains is equiaxed and slightly elongated along the planes perpendicular and parallel to the DPD loading direction, respectively. During subsequent quasi-static compression up to a plastic strain of ~ 0.5 , the shape of grains remained unchanged along both planes.
3. The sample processed by HIP + DPD shows anisotropic mechanical behavior. The sample that was compressed parallel to the impact direction exhibited a long hardening stage followed by a flow stress plateau. At the same time, when the compression axis was perpendicular to the impact direction, softening occurred immediately after a short hardening

regime. Our calculation showed that this anisotropic behavior can be attributed partially to the various values of the Taylor factor along different directions because of the texture formed during DPD and also during subsequent compression. It was also revealed that this effect can result in lower mechanical anisotropy than that observed experimentally. Therefore, other mechanisms such as microstructure destabilization caused by a strain-path change should also be active.

ACKNOWLEDGMENTS

This work was supported in part by the French National Research Agency, ANR (ANR 09-BLAN-0010-01) as well as by Grant No. K-81360 from the Hungarian Scientific Research Fund, OTKA. The European Union and the European Social Fund have provided financial support to the project under the grant agreement TAMOP 4.2.1./B-09/1/KMR-2010-0003.

REFERENCES

1. R.Z. Valiev, R.K. Islamgaliev, and I.V.J. Alexandrov: *Progr. Mater. Sci.*, 2000, vol. 45, pp. 103–89.
2. A.P. Zhilyaev and T.G. Langdon: *Progr. Mater. Sci.*, 2008, vol. 53, pp. 893–979.
3. R.Z. Valiev and T.G. Langdon: *Progr. Mater. Sci.*, 2006, vol. 51, pp. 881–981.
4. Y. Saito, H. Utsunomiya, N. Tsuji, and T. Sakai: *Acta Mater.*, 1999, vol. 47, pp. 579–83.
5. P.E. Armstrong, J.E. Hockett, and O.D. Sherby: *J. Mech. Phys. Solids*, 1982, vol. 30, pp. 37–58.
6. A.P. Zhilyaev, J. Gubicza, G. Nurislamova, A. Révész, S. Surinach, M.D. Baro, and T. Ungar: *Phys. Stat. Solidi*, 2003, vol. 198, pp. 263–71.
7. B. Bay, N. Hansen, D.A. Hughes, and D.K. Wilsdorf: *Acta Metall.*, 1992, vol. 40, pp. 205–19.
8. W.S. Zhao, N.R. Tao, J.Y. Guo, Q.H. Lu, and K. Lu: *Scripta Mater.*, 2005, vol. 53, pp. 745–49.
9. Y. Zhang, N.R. Tao, and K. Lu: *Acta Mater.*, 2008, vol. 56, pp. 2429–40.
10. H.S. Kim and Y. Estrin: *Mater. Sci. Eng. A*, 2008, vols. 483–484, pp. 127–30.
11. D. Jia, K.T. Ramesh, E. Ma, L. Lu, and K.J. Lu: *Scripta Mater.*, 2001, vol. 45, pp. 613–20.
12. S. Billard, J. Fondere, B. Bacroix, and G. Dirras: *Acta Mater.*, 2006, vol. 54, pp. 411–21.
13. D. Witkin, Z. Lee, R. Rodriguez, S. Nutt, and E. Lavernia: *Scripta Mater.*, 2003, vol. 49, pp. 297–302.
14. H.Q. Bui: Ph.D. Dissertation, University of Paris 13, Villetaneuse, France, 2008.
15. M. Legros, B.R. Elliott, M.N. Rittner, J.R. Weertman, and K.J. Hemker: *Philos. Mag. A*, 2000, vol. 80, pp. 1017–26.
16. F. Fellah, G. Dirras, J. Gubicza, F. Schoenstein, N. Jouini, S.M. Cherif, C. Gatel, and J. Douin: *J. Alloys Compd.*, 2010, vol. 489, pp. 424–28.
17. W.Q. Cao, G.F. Dirras, M. Benyoucef, and B. Bacroix: *Mater. Sci. Eng. A*, 2007, vol. 462, pp. 100–105.
18. J. Gubicza, G. Dirras, P. Szommer, and B. Bacroix: *Mater. Sci. Eng. A*, 2007, vol. 458, pp. 385–90.
19. H.Q. Bui, G. Dirras, S. Ramtani, and J. Gubicza: *Mater. Sci. Eng. A*, 2010, vol. 527, pp. 3227–35.
20. A. Abdul-Latif, G.F. Dirras, S. Ramtani, and A. Hocini: *Int. J. Mech. Sci.*, 2009, vol. 51, pp. 797–806.
21. G. Dirras, T. Chauveau, A. Abdul-Latif, S. Ramtani, and H.Q. Bui: *Phys. Stat. Solidi*, 2010, vol. 207, pp. 2233–37.

22. Labotex Software. <http://www.labosoft.com.pl>.
23. G. Ribárik, J. Gubicza, and T. Ungár: *Mater. Sci. Eng. A*, 2004, vols. 387–389, pp. 343–47.
24. L. Balogh, G. Ribárik, and T. Ungár: *J. Appl. Phys.*, 2006, vol. 100, pp. 1–10.
25. G.F. Dirras, J.L. Duval, and W. Swiatnicki: *Mater. Sci. Eng. A*, 1999, vol. 263, pp. 85–95.
26. Y. Iwahashi, Z. Horita, M. Nemoto, and T.G. Langdon: *Acta Mater.*, 1998, vol. 46, pp. 3317–31.
27. M. Kawasaki, Z. Horita, and T.G. Langdon: *Mater. Sci. Eng. A*, 2009, vol. 524, pp. 143–50.
28. G. Dirras, H. Couque, J. Gubicza, A. Abdelouhab, T. Chauveau, and J. Penei: *Mater. Sci. Eng. A*, 2010, vol. 527, pp. 4128–35.
29. G.H. Zahid, Y. Huang, and P.B. Prangnell: *Acta Mater.*, 2009, vol. 57, pp. 3509–21.
30. Y.S. Li, Y. Zhang, N.R. Tao, and K. Lu: *Acta Mater.*, 2009, vol. 57, pp. 761–72.
31. J.C. Glez and J.H. Driver: *Acta Mater.*, 2003, vol. 51, pp. 2989–3003.
32. T. Ungár and J. Gubicza: *Z. Kristallographie*, 2007, vol. 222, pp. 114–28.
33. J. Gubicza, N.Q. Chinh, Z. Horita, and T.G. Langdon: *Mater. Sci. Eng. A*, 2004, vols. 387–389, p. 55.
34. H. Hasegawa, S. Komura, A. Utsunomiya, Z. Horita, M. Furukawa, M. Nemoto, and T.G. Langdon: *Mater. Sci. Eng. A*, 1999, vol. 265, pp. 188–96.
35. N.Q. Chinh, P. Szommer, Z. Horita, and T.G. Langdon: *Adv. Mater.*, 2006, vol. 18, pp. 34–39.
36. W.H. Sillekens, J.H. Dautzenberg, and J.A.G. Kals: *CIRP Ann. Manuf. Techn.*, 1988, vol. 37, pp. 213–16.
37. E.M. Viatkina, W.A.M. Brekelmans, and M.G.D. Geers: *J. Mater. Process. Tech.*, 2009, vol. 209, pp. 186–93.
38. E.V. Nesterova, B. Bacroix, and C. Teodosiu: *Mater. Sci. Eng. A*, 2001, vols. 309–310, pp. 495–99.
39. E.F. Rauch and J.-H. Schmitt: *Mater. Sci. Eng. A*, 1989, vol. 113, pp. 441–48.
40. S. Li: *Scripta Mater.*, 2007, vol. 56, pp. 445–48.
41. Z. Horita, T. Fujinami, and T.G. Langdon: *Mater. Sci. Eng. A*, 2001, vol. 318, pp. 34–41.
42. B.Q. Han, E.J. Lavernia, and F.A. Mohamed: *Metall. Mater. Trans. A*, 2003, vol. 34A, pp. 71–83.
43. W.Z. Han, Z.F. Zhang, S.D. Wu, S.X. Li, and Y.D. Wang: *Phil. Mag. Lett.*, 2006, vol. 86, pp. 435–41.
44. D.J. Alexander and I.J. Beyerlein: *Mater. Sci. Eng. A*, 2005, vols. 410–11, pp. 480–84.
45. R.Z. Valiev and T.G. Langdon: *Progr. Mater. Sci.*, 2006, vol. 51, pp. 881–981.
46. I.J. Beyerlein and C.N. Tomé: *Int. J. Plast.*, 2007, vol. 23, pp. 640–64.
47. T. Ungár, L. Li, G. Tichy, W. Pantleon, H. Choo, and P.K. Liaw: *Scripta Mater.*, 2011, vol. 64, pp. 876–79.
48. C.P. Chang, P.L. Sun, and P.W. Kao: *Acta Mater.*, 2000, vol. 48, pp. 3377–85.
49. N. Dudova, A. Belyakov, T. Sakai, and R. Kaibyshev: *Acta Mater.*, 2010, vol. 58, pp. 3624–42.